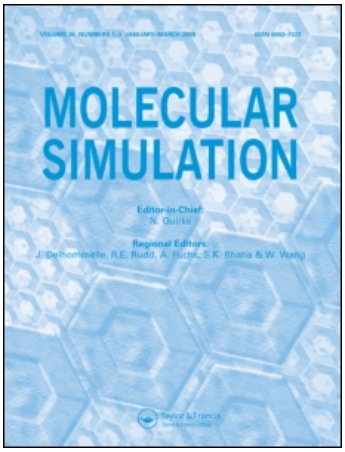

Molecular Simulation
Publication details, including instructions for authors and subscription information:
http://www.informaworld.com/smpp/title~content=t713644482

Nonequilibrium Molecular Dynamics Simulations of *n*-Butane and Isobutane Viscosity

Richard L. Rowley[a]; James F. Ely[b]
[a] Brigham Young University, Utah, USA [b] National Institute of Standards and Technology, Boulder, Colorado, USA

To cite this Article Rowley, Richard L. and Ely, James F.(1991) 'Nonequilibrium Molecular Dynamics Simulations of *n*-Butane and Isobutane Viscosity', Molecular Simulation, 7: 5, 303 — 323
To link to this Article: DOI: 10.1080/08927029108022459
URL: http://dx.doi.org/10.1080/08927029108022459

Molecular Simulation, 1991, Vol. 7, pp. 303–323
Reprints available directly from the publisher
Photocopying permitted by license only

NONEQUILIBRIUM MOLECULAR DYNAMICS SIMULATIONS OF *n*-BUTANE AND ISOBUTANE VISCOSITY

RICHARD L. ROWLEY[1]

Brigham Young University, Provo, Utah, 84602, USA

and

JAMES F. ELY

National Institute of Standards and Technology[2], Boulder, Colorado, 80303, USA

(*Received November 1990, accepted January 1991*)

Nonequilibrium molecular dynamics simulations of Lennard-Jones site–site models representing *n*-butane and isobutane were performed over much of the density range for which experimental viscosity data are available. Simulated viscosities extrapolated to zero shear agreed very well with experimental data over the entire density range. The shear perturbs the equilibrium structure of the fluid and produces shear birefringence or molecular alignment. The relative ability of the molecules to orient in the shear field accounts for their relative shear-thinning rheology. Saturation of the shear birefringence produces a change in the observed rheology at higher shear rates. The effect of shear on thermodynamic properties is also investigated.

KEY WORDS: Molecular dynamics, *n*-butane, isobutane, viscosity, nonequilibrium molecular dynamics, structured molecules, site–site model.

INTRODUCTION

Nonequilibrium molecular dynamics (NEMD) simulations of the viscosity of model fluids are now relatively common [1]. Most of these simulations have focused on simple atomic models with hard-sphere [2], soft-sphere [3,4], screened Coulomb [5] and Lennard-Jones (LJ) [6,7] interaction potentials. (The references shown are intended only as illustrative examples, not as a literature survey.) Far fewer results, however, have been reported for the applications of NEMD to models of structured molecules. Previous NEMD studies of structured molecules have generally been restricted to a few conditions for a single fluid. For example Edberg *et al.* [8] performed simulations at three state points for *n*-butane and at a single condition for *n*-decane. Little has been done to establish the efficacy of these models over a wide range of conditions for real fluids or to examine the effects of a structure on the simulated viscosity. This is primarily because representation of the structure of a molecule with site potentials requires CPU time roughly proportional to n_s^2, where n_s

[1] On leave at National Institute of Standards and Technology in Boulder, Colorado, during the course of this work.

[2] United States Government agency – this paper not subject to copyright in the United States.

is the number of sites per molecule. This additional computational time, coupled with the necessity to perform simulations at several shear rates in order to obtain by extrapolation the zero-shear viscosity at each condition, makes the NEMD simulations of structured molecules over a range of conditions an ambitious task. Additionally, reduced time steps and longer simulations are often required for simulations of structured molecules in order to maintain stability of the integration routines and to compute accurate properties.

In this study, structured models for *n*-butane and isobutane are used to simulate viscosities over a wide range of densities. Simulated data are compared to experimental data at the same conditions. Such an extensive simulation project first requires implementation of several time-saving techniques. These modifications of the NEMD method of constraints [9] were introduced in a companion paper [10]. In that study, it was found that purely structural effects were incapable of producing the difference in viscosities experimentally observed between *n*-butane and isobutane when modeled with the same LJ site parameters. However, increasing the size of the LJ site size, σ, by only 2.5% did produce viscosities in good agreement with experimental data. In this paper, these models are used to further explore the nonequilibrium structure of the fluid and its effect on the viscosity and thermodynamic properties of the pure fluids.

SIMULATIONS

Molecular Models

An effective four-site model for *n*-butane molecules has been previously tested and used in MD simulations [8,10,11]. The model molecule is composed of four equivalent methyl/methylene sites located at carbon centers. Interactions between sites of different molecules were modeled with standard 12-6 LJ potentials. Distances between neighboring sites were constrained to 0.153 nm, and bond angles were fixed at 109.47° by a next-nearest-neighbor distance constraint. All intramolecular interactions were obtained from the Ryckaert-Bellemans [11] potential which has proven effective in modeling conformational populations and interconversions [8,11–13]. Table 1 summarizes the model parameters used. While slightly different values of the LJ parameters have also been used in simulations of *n*-butane [12–16], the values of Table 1 were selected because of the excellent representation of viscosity obtained by Edberg *et al.* [8] using them.

Isobutane was similarly modeled with four equivalent LJ sites located at the physical carbon centers. Except for σ, the parameters for this model, also shown in Table 1, are identical to those used in the *n*-butane model. The σ value shown in Table 1 was obtained [10] by adjusting it until agreement was obtained between simulated and experimental viscosites at a single density. As in the case of *n*-butane, isobutane molecules were considered rigid with bond lengths and angles fixed at the values shown in Table 1.

Equations of Motion

Nonequilibrium MD simulations were performed using a NVT (canonical ensemble) algorithm developed by Edberg *et al.* [9], a molecular version of the isothermal shear

Table 1 Model parameters

parameter	*units*	n-*butane*	*isobutane*
m	kg	2.41×10^{-26}	2.41×10^{-26}
d (bond distance)	nm	0.153	0.153
θ (bond angle)	degrees	109.47	109.47
ε/k	K	72	72
σ	nm	0.3923	0.4020

algorithm known as SLLOD [17,18]. Rather than solve Newtonian equations of motion subject to constraints as popularized by the SHAKE algorithm [19], non-Newtonian equations of motion which naturally include the constraint forces are derived following the prescription of Gauss's principle of least constraint [9,18,20]. A principal advantage of this method for the type of problem considered here is that all of the constraints imposed by the fixed bond distances, the isothermal thermostat and the applied shear field are similarly and efficiently incorporated into the equations of motion as additional force terms. This makes implementation of the method into standard MD programs relatively straightforward. Newtonian forces, F^N, can be calculated from relative site positions in the standard way, the constraint forces, F^C, can be obtained from Gauss's principle, and the usual integration algorithms may be used to trace the particle trajectories in phase space using the total force, $F^N + F^C$. The equations of motion and the bond constraint matrices used in this work are given in the Appendix. Derivation of the equations and discussion of the method are available in references [8] and [9].

Viscosity Simulations

NVT simulations were performed on three-dimensional systems of 125 molecules using a cut-off distance of 2.5σ with appropriate long-range corrections. The geometry used is schematically shown in Figure 1 and the constant applied shear rate γ in the simulations is defined with respect to these Cartesian coordinates and the x component of velocity as

$$\gamma = \left(\frac{\partial v_x}{\partial y}\right). \tag{1}$$

All simulations were performed on a Cyber* 205 supercomputer using the automatic vectorization options of the resident FORTRAN compiler. The dimensionless time step size was chosen to be 0.0015, corresponding to 2.9 fs in real time. Between 60 000 and 120 000 time steps beyond "equilibration" were used to obtain property time averages. All production runs were started from configuration files of previous simulations by changing the run conditions or shear rate. This generally shortened the time required to "equilibrate" or stabilize the simulated properties to about 20 000 time steps.

* Brand names and commercial sources of materials and instruments are given for scientific completeness and comparison purposes. Such information does not constitute endorsement of these products or imply their superiority over other available brands.

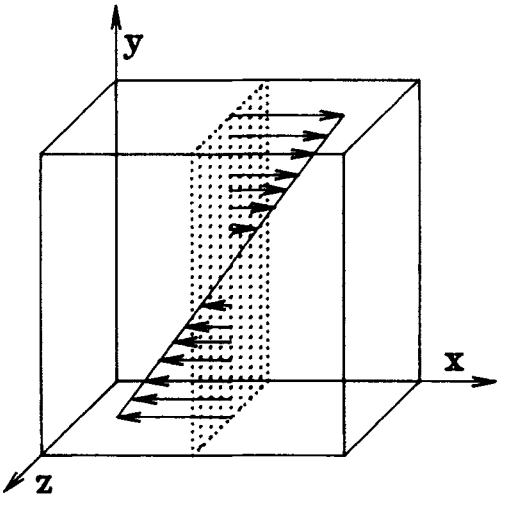

Figure 1 Schematic showing the linear velocity profile or constant shear rate in relation to the coordinate system used in the simulations.

A previous NEMD code based on Gaussian mechanics and bond constraints [8] was significantly modified to make this study tractable by adaptation of known EMD time-saving algorithms. The final code ran about 11 times faster than the original. The algorithms and their time-saving benefits are summarized in the Appendix.

Bulk properties of the fluid were computed with the standard time averages of appropriate dynamical variables. The system temperature, T, was constrained to be a constant of motion, formulated in terms of the molecular mass, M, the number of molecules, N, Boltzman's constant, k, and center-of-mass momentum, $\boldsymbol{p}$, as

$$T = \sum_i \frac{\boldsymbol{p}_i^2}{M(3N - 4)k} \tag{2}$$

where the usual $3N$ degrees of freedom have been reduced by 4 due to the requirements of momentum conservation in each of the three directions and the constraint imposed on the sum of squared momenta by the constant temperature algorithm. The virial theorem defines the molecular pressure tensor as

$$P = \frac{1}{V}\sum_i (\boldsymbol{p}_i\boldsymbol{p}_i/M + \boldsymbol{r}_i\boldsymbol{F}_i). \tag{3}$$

where V is volume and $\boldsymbol{r}_i$ is the position vector of molecule i. The hydrostatic pressure is obtained from $(1/3)Tr(\mathbf{P})$, and the nonlinear shear viscosity, $\eta(\gamma)$, is computed from the constitutive relation,

$$\eta(\gamma) = -\frac{1}{\gamma}\left\langle \frac{1}{2}P_{yx} + \frac{1}{2}P_{xy} \right\rangle. \tag{4}$$

It can be shown from linear response theory that $\eta(\gamma)$ defined in Equation (4) reduces to the standard Green-Kubo relation for the zero shear rate viscosity in the limit $\gamma \to 0$ [9]. Thus, extrapolation of $\eta(\gamma)$ to $\gamma = 0$ gives the Green-Kubo viscosity, $\gamma(0)$.

The asymptotic behavior for $\eta(\gamma)$ [21–23]

$$\eta(\gamma) = \eta(0) - A\gamma^{1/2} \tag{5}$$

is generally used to perform the extrapolation [7,23].

Simulations were performed at dimensionless conditions corresponding to those of available experimental data [24]. Properties were made dimensionless in terms of site parameters. Thus,

$$T^* = \frac{kT}{\varepsilon}, \quad \eta^* = \eta \frac{\sigma^2}{(m\varepsilon)^{1/2}}, \quad P^* = P\frac{\sigma^3}{\varepsilon}, \quad \gamma^* = \gamma\sigma\left(\frac{m}{\varepsilon}\right)^{1/2}. \tag{6}$$

where ε is the LJ energy parameter and m is the site mass. Likewise, the site number density, ρ, is four times the molecular number density, or

$$\rho^* = \rho\sigma^3 = \frac{4N\sigma^3}{V}. \tag{7}$$

To ascertain the dependence of simulated viscosity on shear rate, simulations were performed at several shear rates in the range $0.04 \leq \gamma^* \leq 1.0$. Figure 2 shows the results of these simulations for both *n*-butane and isobutane at the same dimensionless conditions $T^* = 1.871$ and $\rho^* = 1.85$. Note that η^* appears quite linear with $\gamma^{*1/2}$ over the range $0 \leq \gamma^* \leq 0.16$, but that the rheology of the two fluids is different for larger values of γ^*. While both fluids are shear-thinning in the low shear region, η^* seems nearly independent of γ^* in the range $0.25 \leq \gamma^* \leq 1.0$. This agrees with previous findings [8] in which a shear-thinning (for $0 < \gamma^* < 0.25$), an approxi-

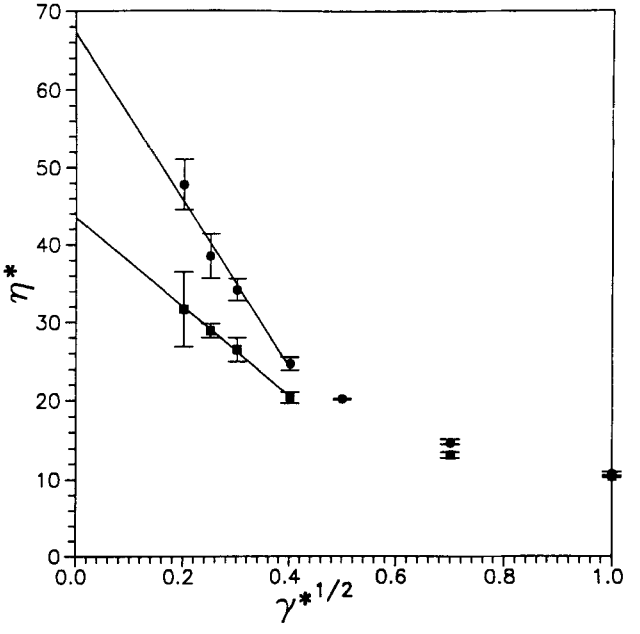

Figure 2 Difference in rheological behavior of *n*-butane (●) and isobutane (■) at $T^* = 1.871$ and $\rho^* = 1.85$. Uncertainty bars are estimated from the standard deviation of shorter sequential simulations.

mately Newtonian (for $0.25 < \gamma^* < 1$), and a subsequent shear-thinning (for $\gamma^* > 1$) regime were all noted for $\eta(\gamma)$ of *n*-butane. The rheology of isobutane is seen to be similar to that of *n*-butane in Figure 2, although *n*-butane is significantly more shear thinning than isobutane in the first region. The error bars shown in this figure are only relative estimates calculated from the standard deviations of between 4 and 8 successive 15 000 time-step portions of the total simulation.

The appearance of two different rheological regions at relatively low shear rates is different for these structured model molecules than the behavior observed in simulation of simple LJ fluids. In the latter case, excellent agreement with Equation (5) has been observed for $\gamma^* < 3$ at which point nonlinear behavior is observed [6–23]. It is evidently essential to investigate the region over which Equation (5) is valid for multiple site LJ models before linear extrapolation is used to obtain $\eta^*(0)$. This is not always easy and may require additional simulations. For example, Wang and Cummings [7] used Equation (5) over the range $0 < \gamma^* < 1.4$ to obtain $\eta^*(0)$ for single-, two- and three-site models of CO_2. Only two of their five simulation points are at the lower γ^* values where this work suggests Equation (5) is valid for the four-site butane models. While statistically their data for the two- and three-site model cannot be used to either confirm or exclude the possibility of a change in slope of $\eta^*(\gamma^*)$, it is interesting that considerably better agreement with experimental values are obtained for these CO_2 models if only the two lower γ^* values are used to perform the linear extrapolation to $\gamma^* = 0$.

The value for $\eta^*(0)$ was generally obtained from a weighted linear least squares fit of simulated values at $\gamma^{*1/2} = 0.2, 0.25, 0.3$ and 0.4. Weights were obtained from the

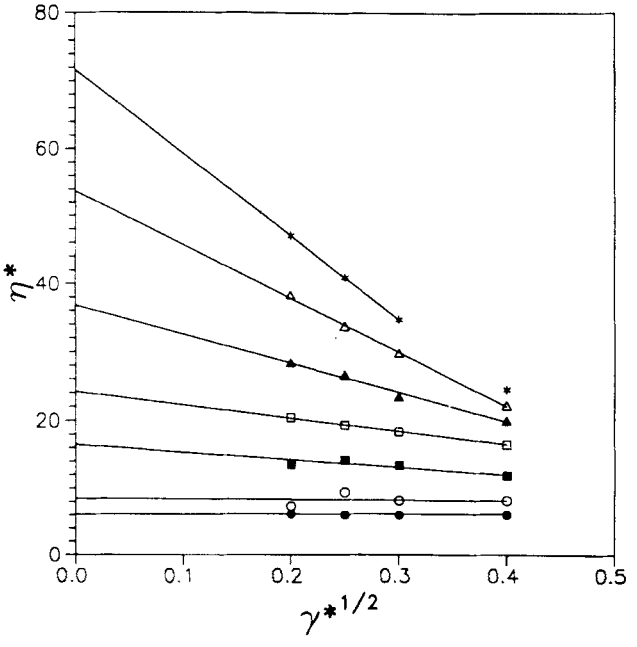

Figure 3 Results of *n*-butane simulations for $\eta^*(\gamma^{*1/2})$ at $\rho^* = 1.50$ (●), $\rho^* = 1.60$ (○), $\rho^* = 1.70$ (■), $\rho^* = 1.75$ (□), $\rho^* = 1.80$ (▲), $\rho^* = 1.83$ (△) and $\rho^* = 1.85$ (*). Lines represent weighted least squares fits through data shown.

standard deviations of replicate runs at each shear rate. Larger uncertainties are obtained for smaller γ^* values. For $\gamma^{*1/2} < 0.2$ the uncertainties in η^* are large enough to counterbalance their usefulness in extrapolating to $\gamma = 0$. Simulated values as a function of shear rate for the runs are shown in Figures 3 and 4 along with the least squares fit of the data. At very high liquid densities, above about $\rho^* = 1.8$, the region linear in $\gamma^{*1/2}$ was found to contract to lower shear rates. For example, at the highest densities used for isobutane simulations, only shear rates for $\gamma^{*1/2} \leq 0.2$ could be safely assumed to be in the linear region. Values at even lower shear rates were required to supplement these extrapolations as shown in Figure 4, in spite of the larger uncertainties at the lower shear rates. The simulations at $\rho^* = 1.99$ roughly represents the upper limit at which linear extrapolation to $\gamma^* = 0$ is useful due to the narrowing of the linear region.

RESULTS

Values for $\eta^*(\gamma)$ obtained from the simulations are tabulated in Tables 2 and 3. Also shown in these tables are the values of $\eta^*(0)$ obtained from the extrapolation procedure described above and from the experimental data [24]. A comparison of the density dependence of simulated and experimental η values is shown in Figure 5. Simulated values agree remarkably well with the experimental data over the entire accessible density range.

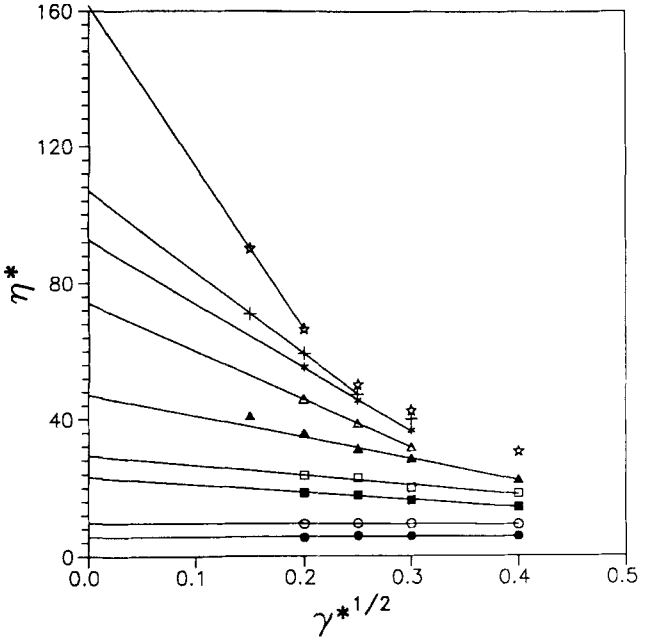

Figure 4 Results of isobutane simulations for $\eta^*(\gamma^{*1/2})$ at $\rho^* = 1.55$ (●), $\rho^* = 1.68$ (○), $\rho^* = 1.80$ (■), $\rho^* = 1.85$ (□), $\rho^* = 1.90$ (▲), $\rho^* = 1.93$ (△), $\rho^* = 1.95$ (*), $\rho^* = 1.97$ (+) and $\rho^* = 1.99$ (☆). Lines represent weighted least squares fits through data shown.

Table 2 Results of *n*-butane simulations

T^*	ρ^*	η^* $\gamma^* = 0.16$	η^* $\gamma^* = 0.09$	η^* $\gamma^* = 0.0625$	η^* $\gamma^* = 0.04$	$\eta^*(0)$ (sim)	η^* (exp)
3.82	1.50	6.00	5.93	6.03	6.11	6.12	6.3
3.472	1.60	8.14	8.14	9.39	7.26	8.53	9.6
2.778	1.70	11.89	13.37	14.19	13.50	16.53	16.8
2.5	1.75	16.51	18.38	19.34	20.44	24.22	23.9
2.22	1.80	20.0	23.4	26.6	28.4	36.8	37.6
2.03	1.83	22.2	29.8	33.7	38.3	53.7	53.0
1.944	1.85	24.5[a]	34.7	40.9	47.0	71.6	73.0

[a] Value not used in linear extrapolation to $\gamma = 0$.

Table 3 Results of isobutane simulations

T^*	ρ^*	η^* $\gamma^* = 0.16$	η^* $\gamma^* = 0.09$	η^* $\gamma^* = 0.0625$	η^* $\gamma^* = 0.04$	η^* $\gamma^* = 0.0225$	$\eta^*(0)$ (sim)	η^* (exp)
4.167	1.55	5.76	5.76	5.89	5.35		5.7	5.50
3.472	1.68	9.22	9.45	9.58	9.35		9.8	9.57
2.778	1.80	14.37	16.44	17.92	18.63		23.3	19.0
2.5	1.85	18.3	20.1	22.9	23.7		29.4	27.8
1.944	1.90	22.38	28.44	31.32	35.7	40.9	47.1	46.0
1.875	1.93		31.7	38.7	45.9		74.2	75.2
1.667	1.95		36.6	45.5	55.3		92.7	100
1.736	1.97		39.9[a]	47.3	59.4	70.9	107	144
1.736	1.99	30.5[a]	42.6[a]	50.2[a]	66.6	90.3	161	182

[a] Value not used in extrapolation to $\gamma = 0$.

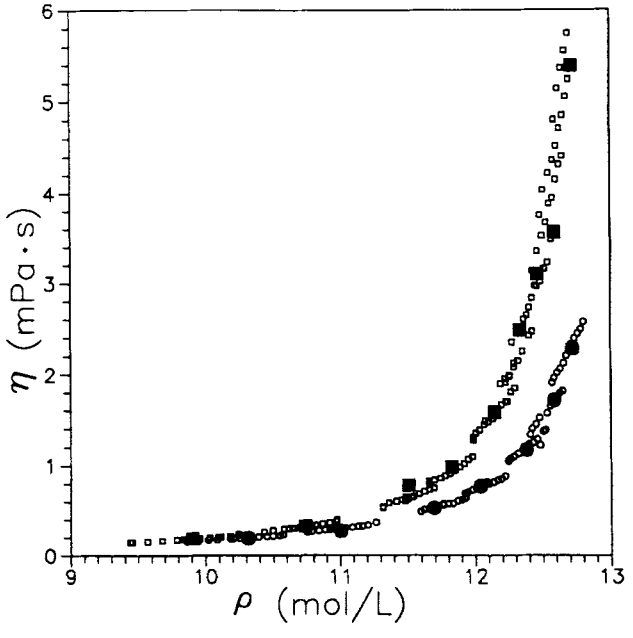

Figure 5 Comparison of simulated η values (solid symbols) to experimental data (open symbols) [24] for *n*-butane (●, ○) and isobutane (■, □) at same conditions as Figure 2.

The effect of shear on P^* is shown in Figures 6 and 7. To within the uncertainty of the simulated values, the values in the low shear region appear to obey the asymptotic behavior represented by [21–23],

$$P(\gamma) = P(0) + B\gamma^{3/2}. \tag{8}$$

However, the combination of uncertainty in the simulated values and the relatively small range over which Equation (5) holds, make it impossible to confirm Equation (8); one can only say that the simulations are consistent with this equation. Evans *et al.* [23] suggest that the value of the pressure obtained from NEMD has less statistical uncertainty than the corresponding value determined from EMD. Because simulations in this work were started from previous configuration files, only one EMD simulation was performed for each of the two fluids. Both of these EMD pressures were lower than the $P^*(0)$ values obtained from Equation (8), though the deviation was only slightly larger than the combined uncertainty limits of the two. Wang and Cummings [7] found that experimental CO_2 pressures were significantly lower than the values extrapolated from NEMD simulations; no EMD simulations were reported. While the consistency between the lower experimental pressure (relative to $P^*(0)$ from NEMD) in that study and the lower EMD P^* found in this work may be purely coincidental, it is an interesting consistency that should be investigated in future work. Unfortunately, at the high liquid densities of interest in this work, the ρ-P isotherms are so steep that pressures from equations of state and interpolated from experimental data are not accurate enough for a comparison to the simulated data.

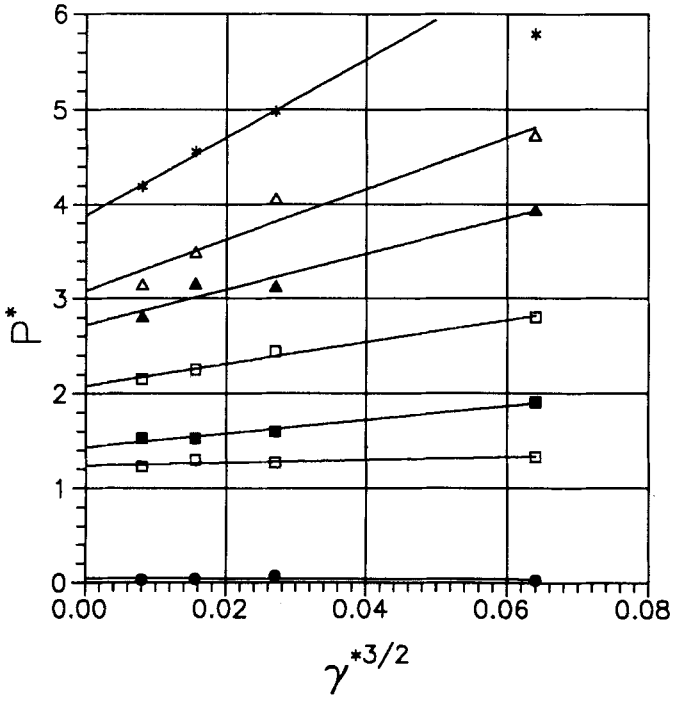

Figure 6 Shear dependence of system pressure for *n*-butane. Symbols have the same significance as in Figure 3.

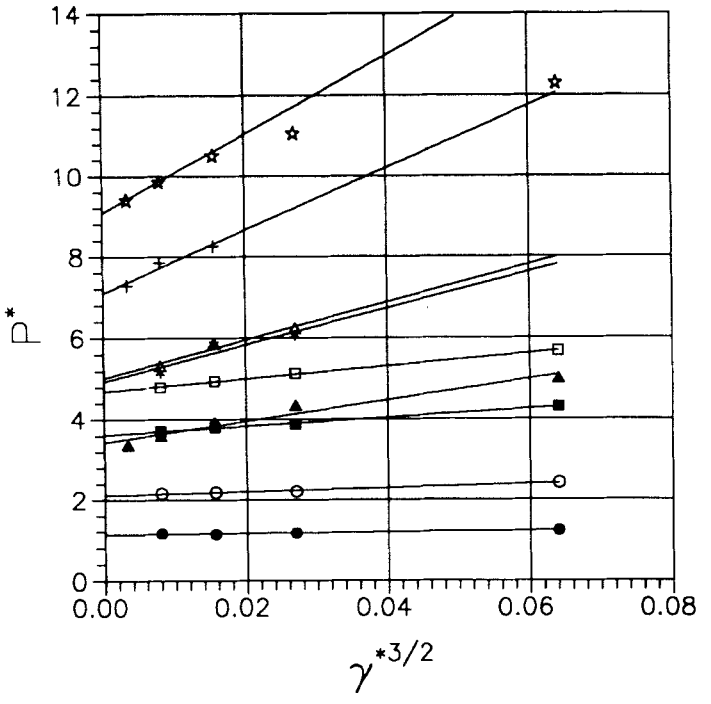

Figure 7 Shear dependence of system pressure for isobutane. Symbols have the same significance as in Figure 4.

Over the same region for which $\eta^*(\gamma^*)$ was found to follow Equation (5), $P^*(\gamma^*)$ appears to obey Equation (8). Pressures in the second rheological region at higher shear rates apparently also deviate from this behavior as can be seen at the highest density in Figure 7. Simulations on a two-dimensional soft-disc liquid [23] indicate that at very low shear rates P^* is nearly independent of γ^*; i.e., the value of B in Equation (8) changes to zero at some transition point. Although there is no indication of similar behavior in this study, the lowest shear rates used are still larger than those suggested as the transition point. Nevertheless, a leveling of P^* with respect to $\gamma^{*2/3}$ would produce an even larger simulation value for $P^*(0)$.

Figures 8 and 9 show simulated values of internal energy, E^* ($E^* = E/\varepsilon$), plotted vs. $\gamma^{*3/2}$ as suggested by theory,

$$E(\gamma) = E(0) + C\gamma^{3/2}. \tag{9}$$

Again the results are in agreement with the simple $\gamma^{*3/2}$ dependence, though other functionalities are not ruled out by the data. Interestingly, the total internal energy is much flatter than that usually observed for LJ fluids [7,23]. As seen in Figure 10, this is due to the competing effects of the energy due to the intermolecular and intramolecular interactions.

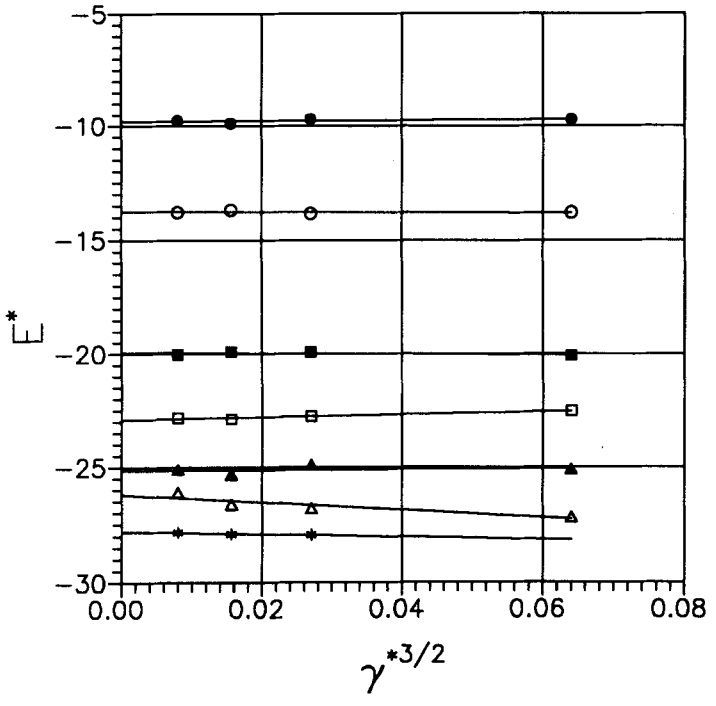

Figure 8 Shear dependence of internal energy for *n*-butane. Symbols have the same significance as in Figure 3.

DISCUSSION

The greater shear-thinning behavior of *n*-butane relative to that of isobutane observed in Figures 2–4 can be understood in terms of molecular structure. Consider first the case of *n*-butane. The shear force distorts the equilibrium structure as is evident in the computed radial distribution function $g(r^*)$ shown in Figure 11. Neighboring molecules are forced out of equilibrium positions by the shear. The well-known dilation effect of the shear in constant pressure systems is also a direct result of the tendency for the shear to move molecules out of equilibrium positions into various y planes. The shear also propels upstream molecules from their equilibrium positions further into the repulsive part of the potential. These effects produce the shear dependences observed for the energy and pressure in Figures 6–10. They also shift the first peak of $g(r^*)$ in Figure 11 to a lower r^* value. Just as molecules upstream are driven into the potential of a reference molecule, molecules downstream are pulled further out in the potential by the shear. The shoulder on the first peak is due to these asymmetries produced by the shear.

The shear force also produces alignment of the molecules. Histograms of bond vectors show [10] increasing alignment as the shear rate is increased until an orientational saturation occurs. This shear-induced alignment can also be monitored in terms of the symmetric order tensor

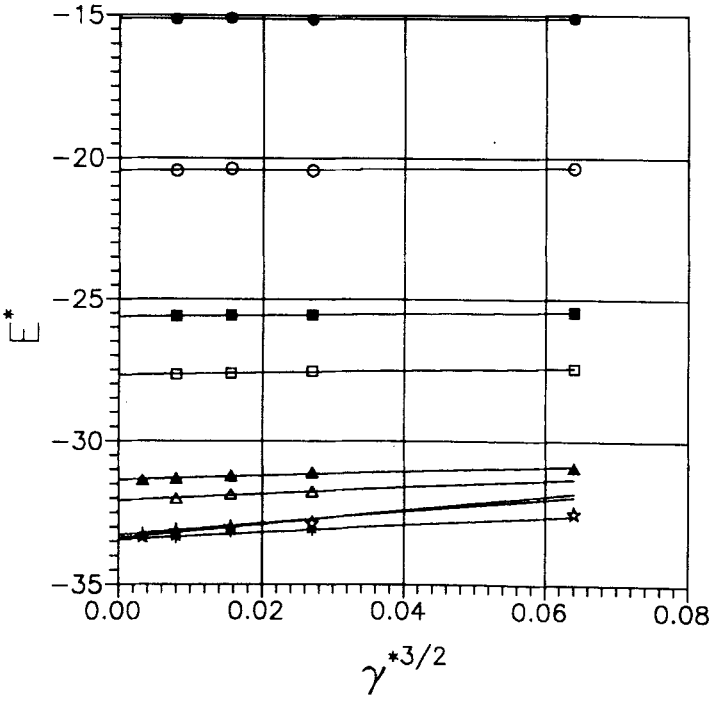

Figure 9 Shear dependence of internal energy for isobutane, Symbols have the same significance as in Figure 4.

$$S = \frac{\sum_i \boldsymbol{R}_i \boldsymbol{R}_i}{N} \tag{10}$$

where the arbitrary orientation vector $\boldsymbol{R}_i$ is taken to be the end-to-end vector $\boldsymbol{e}_i$ for *n*-butane molecules and the bond vector $\boldsymbol{b}_i$ between a methyl group (site 1) and the central -CH group (site 2) for isobutane molecules. It is convenient to examine this ordering effect in terms of the normalized birefringence or order tensor, $\mathbf{S}^\circ = \mathbf{S}/Tr(\mathbf{S})$. In an orientationally isotropic fluid $\mathbf{S}^\circ = 1/3\mathbf{I}$. Shown in Figure 12 are the *xx* and *yy* components of $\mathbf{S}^\circ$ again indicating that the shear produces preferential orientation. From this figure it is apparent that the increasing alignment of the molecules in the shear field is a primary cause of the shear thinning region noted in Figure 2. The second rheological region in which the fluid viscosity is nearly independent of γ occurs when the orientational alignment is saturated. This is seen from Figures 2 and 12 to occur at about $\gamma^* = 0.25$.

The alignment capability of isobutane due to a shear field is somewhat different than that of *n*-butane because of the inherent symmetry within the molecules. For isobutane, the diagonal elements of $\mathbf{S}^\circ$ are all nearly 1/3, independent of the shear rate. There is a slight orientation of the molecules as indicated by the nonzero off-diagonal element S°_{xy}, shown in Figure 13, which again saturates at about $\gamma^* = 0.25$.

As observed in Figure 2, the branched nature of isobutane produces a viscosity lower than that of *n*-butane at equivalent reduced conditions. Figure 2 indicates that

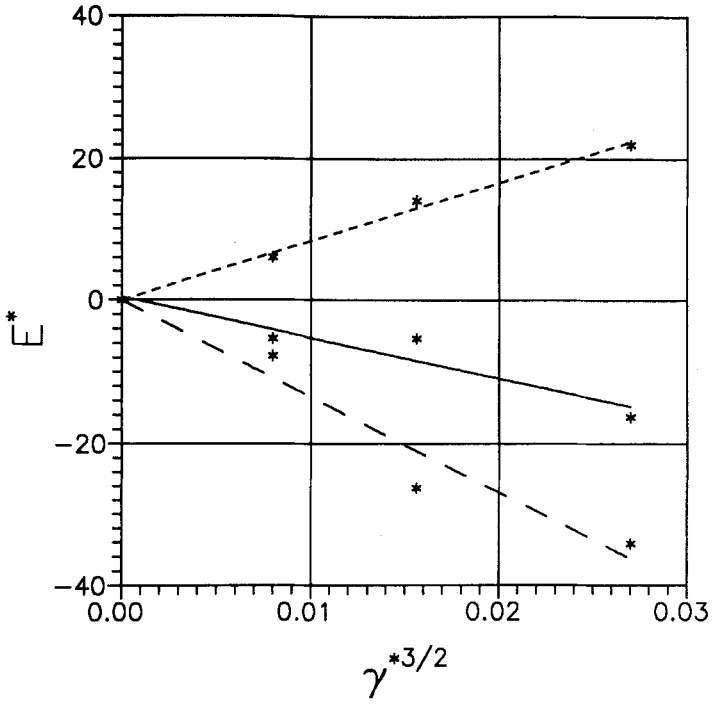

Figure 10 Shear dependence of intramolecular energy (– – –), intermolecular energy (— — —) and internal energy (———) for *n*-butane at $\rho^* = 1.85$. Values are shown relative to the value at $\gamma^* = 0$.

the reduced viscosities are nearly equivalent at shear rates high enough to saturate molecular alignment capabilities within the fluid. It therefore seems likely that the higher reduced viscosity of *n*-butane at the lower shear rates is due to the extension of some of the chains over a wider range of shear rates in the *y* direction because of the random orientations. An alternative way of stating this is that the more branched molecule does not produce as much drag as the longer chain molecules, some of which orient perpendicular to the shear. At higher shear rates where orientational saturation occurs, the viscosities become approximately equivalent as the relatively lower alignment ability of the isobutane molecules takes its toll. A graphical simulation at $\gamma^* = 1.0$ shows that oriented *n*-butane molecules are capable of a more independent movement in *y*-layers because the protruding methyl groups of the isobutane molecules tend to extend to different layers, locking the fluid into a more collective movement.

Though not really discernible from Figure 2, larger error bars were usually observed for the *n*-butane simulations than for isobutane. This was attributed to extra intramolecular degrees of freedom in *n*-butane and the *trans/gauche* isomer fluctuations. The number of *trans* conformers were monitored during the simulations. The kinetics of the conformational changes were observed to be slow relative to the "equilibration" of other properties; approximately 100 000 integration steps were required from a cold start before the *trans/gauche* conformation ratio became stable. Starting production runs from previous run configuration files generally shortened this conformational relaxation time to 20 000–40 000 time steps. The conformational

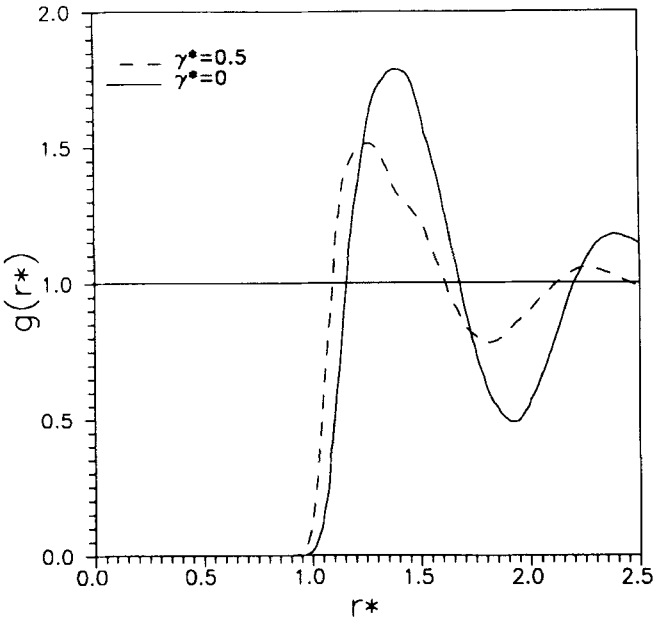

Figure 11 Radial distribution function for *n*-butane at the conditions of Figure 2 at equilibrium (——) and under shear ($\gamma^* = 0.5$, - - -).

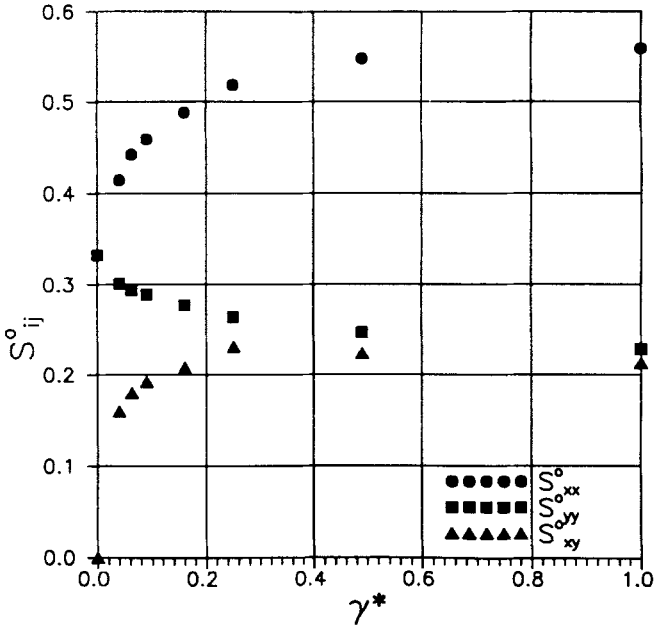

Figure 12 Components of normalized order tensor for *n*-butane at conditions of Figure 2.

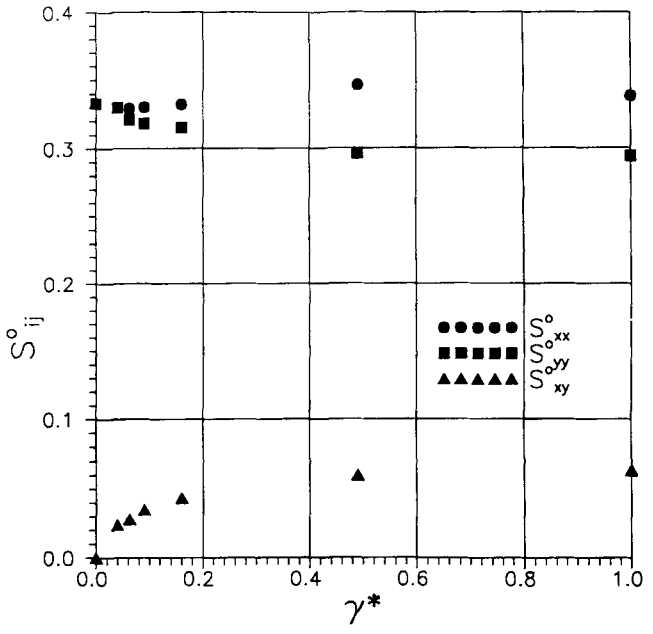

Figure 13 Components of normalized order tensor for isobutane at conditions of Figure 2.

equilibrium constant was perturbed by the applied shear field, the *trans* form being favored at higher shear rates. The equilibrium percentage of the *trans* isomer has been investigated previously [8,14,25–27]. No correlation of percent *trans* as a function of state has yet been deduced, but values in the literature generally range from 50 to 61% at various conditions. Our simulations with $\gamma^* = 0$ produced 58 $\pm$ 1.5% *trans* in good agreement with many of the values previously reported at similar conditions. The *trans* population increased to as high as 86% at the higher shear rates. Observation of the apparent viscosity during the stabilization of the conformation population ratio indicates that conformational changes do have a small effect on the observed viscosity, but the effect is much smaller than the previously mentioned effect due to molecular alignment.

CONCLUSIONS

Our NEMD simulations of *n*-butane and isobutane modeled as rigid, four equivalent site molecules are in excellent agreement with experimental data over the entire density range accessible to us by simulation. In obtaining η values for structured molecules, care must be taken to determine the region over which linear extrapolation to zero shear is valid. This region is different for structured molecules than simple LJ fluids. Moreover, the linear region is a function of density, and may become quite narrow at very high liquid densities.

The rheology and shear-dependence of the viscosity and thermodynamic properties can be interpreted in terms of the inherent structural differences of the two molecules. The structure of the fluid under shear is different than the equilibrium structure.

Moreover, the shear produces molecular orientational preferences observed as shear-induced birefringence. The difference in alignment capability of the two molecules accounts for the difference in shear-thinning observed in the simulations. Saturation of the alignment produces the change from shear-thinning to nearly constant viscosity with increasing γ. The effect of shear on pressure and internal energy are similarly affected by the nonequilibrium structure of the fluid and the orientability of the molecules. Theoretical-based linear relations between E^*, P^* and η^* and γ^* are consistent with the simulations over the range of shear before the birefringence saturation occurs.

APPENDIX

NEMD Algorithm

Gauss's principle of least constraint provides an exact prescription for obtaining equations of motion involving holonomic constraints. We follow the notational convention of Edberg *et al.* [9] for convenience so that our constraint matrices are of the same form. The equations of motion for site α in molecule i are

$$\dot{\boldsymbol{r}}_{i\alpha} = \boldsymbol{p}_{i\alpha}/m_\alpha + \boldsymbol{n}_x \gamma y_i, \tag{11}$$

$$\dot{\boldsymbol{p}}_{i\alpha} = \boldsymbol{F}_{i\alpha}^N + \boldsymbol{F}_{i\alpha}^C - \boldsymbol{n}_x (m_\alpha/M)\gamma p_{yi} - \zeta \boldsymbol{p}_i. \tag{12}$$

Molecular quantities appearing in the above equations are defined in terms of the constituent site quantities by the relations

$$M = \sum_\alpha m_\alpha, \quad \boldsymbol{r}_i = \sum_\alpha m_\alpha \boldsymbol{r}_{i\alpha}/M, \quad \boldsymbol{p}_i = \sum_\alpha \boldsymbol{p}_{i\alpha}, \quad \text{and} \quad \boldsymbol{F}_i = \sum_\alpha \boldsymbol{F}_{i\alpha}. \tag{13}$$

Force superscripts N and C denote, respectively, Newtonian interparticle forces and constraint forces which maintain bond lengths and bond angles within the molecule. The terms containing γ impose a strain rate, $\gamma = \partial u_x/\partial y$, in the y direction (see Figure 1), and $\boldsymbol{n}_x$ is a unit vector in the x direction. The molecular thermostat multiplier, ζ, represents the constraint force required to maintain isothermal conditions.

The undetermined multipliers for each of the constraint forces in Equations (11) and (12) are determined by substituting the equations of motion into the differential form of the constraint equations. For example, the holonomic bond constraint between two sites is

$$h_{\alpha\beta} = \boldsymbol{r}_{\alpha\beta}^2 - d^2 = 0. \tag{14}$$

where $\boldsymbol{r}_{\alpha\beta} = \boldsymbol{r}_\beta - \boldsymbol{r}_\alpha$ and d is the fixed bond length. In Gauss's formalism, the constraint equation $h(\boldsymbol{r}, \dot{\boldsymbol{r}}, t) = 0$ can always be put into the differential form involving the scalar function s

$$\boldsymbol{n}(\boldsymbol{r}, \dot{\boldsymbol{r}}, t) \cdot \ddot{\boldsymbol{r}} = s(\boldsymbol{r}, \dot{\boldsymbol{r}}, t) \tag{15}$$

by differentiating the constraint equation once for nonholonomic and twice for holonomic constraints. Equation (15) defines a hyperplane in acceleration space with its normal vector $\boldsymbol{n}$. Constrained acceleration vectors must terminate on the hyperplane defined by this equation in order to satisfy the constrained equations of motion; the constraint force projects the Newtonian acceleration onto the constraint hyperplane. While there are an infinite number of ways to project an arbitrary acceleration

vector onto the constraint acceleration hyperplane, the normal projection minimizes the magnitude of the constraint force in accordance with Gauss's principle of least constraint. The differential form of the bond constraint equation is

$$\boldsymbol{r}_{\alpha\beta} \cdot \ddot{\boldsymbol{r}}_{\alpha\beta} + (\dot{\boldsymbol{r}}_{\alpha\beta})^2 = 0. \tag{16}$$

Thus, the bond vectors $-\boldsymbol{r}_{\alpha\beta}$ and $\boldsymbol{r}_{\alpha\beta}$ are seen to be the normal vectors in $\ddot{\boldsymbol{r}}_\alpha$ and $\ddot{\boldsymbol{r}}_\beta$ space, respectively, and the constraint forces required to project the Newtonian force back onto the constrained acceleration hyperplane must be multiples of these normals, or $\boldsymbol{F}_\alpha^C = -\lambda \boldsymbol{r}_{\alpha\beta}$ and $\boldsymbol{F}_\beta^C = \lambda \boldsymbol{r}_{\alpha\beta}$. If Equation (12) is substituted into Equation (16), one can solve for λ. In this example of a single bond constraint between two sites,

$$\lambda = -\frac{\boldsymbol{F}_{\alpha\beta}^N \cdot \boldsymbol{r}_{\alpha\beta} + \dot{r}_{\alpha\beta}^2}{2r_{\alpha\beta}^2}. \tag{17}$$

As long as λ is obtained at each time step from Equation (17), Equations (11) and (12) describe the proper trajectory of two sites constrained to move with a fixed bond distance.

Generalization of the bond constraint equations to the case of *n*-butane and isobutane, in which fixed bond angles and bond distances between neighboring sites and next-nearest neighbor sites impose multiple constraints, yields a matrix form of Equation (12),

$$\ddot{\boldsymbol{r}}_\alpha = \boldsymbol{F}_\alpha + \sum_i M_{\alpha n}(\lambda \boldsymbol{R}_n), \tag{18}$$

where the matrix M applies the appropriate constraints from the column vector $(\lambda \boldsymbol{R})_n$ for each site α. Here, the notation of Edberg *et al.* [9] has been retained where $\boldsymbol{R}_n = \boldsymbol{r}_{\alpha\beta} = \boldsymbol{r}_\beta - \boldsymbol{r}_\alpha$, with $n = \alpha + \beta - 2$ and all site masses set to unity. In this numbering scheme, nearest-neighbor vectors have odd values of n, while next-nearest-neighbor vectors have even values. The interested reader should see reference [9] for specific details on the constraint matrices and their implementation. The constraint matrices used for *n*-butane and isobutane were

$$M_{\text{butane}} = \begin{bmatrix} -1 & -1 & 0 & 0 & 0 \\ 1 & 0 & -1 & -1 & 0 \\ 0 & 1 & 1 & 0 & -1 \\ 0 & 0 & 0 & 1 & 1 \end{bmatrix} \tag{19}$$

and

$$M_{\text{isobutane}} = \begin{bmatrix} -1 & -1 & 0 & 0 & 0 & -1 \\ 1 & 0 & -1 & -1 & 0 & 0 \\ 0 & 1 & 1 & 0 & -1 & 0 \\ 0 & 0 & 0 & 1 & 1 & 1 \end{bmatrix}, \tag{20}$$

respectively. Note that the bond constraint matrix for isobutane contains an additional column. M is a $n_s \times n_c$ matrix (n_c is the number of constraints). For n-butane, $n_c = 2n_s - 3$; $n_c = 2n_s - 2$ for isobutane.

The Gaussian thermostat is essential to this NEMD algorithm because it removes heat produced irreversibly by the shear. The differential form of the temperature constraint [Equation (2)] is

$$\dot{T} = \sum_i \boldsymbol{p}_i \cdot \dot{\boldsymbol{p}}_i = 0. \tag{21}$$

By substituting Equation (12) into (21) and summing over sites α, one can show that

$$\zeta = \frac{\sum_i \boldsymbol{p}_i \cdot \boldsymbol{F}_i - \gamma \sum_i p_{xi} p_{yi}}{4 \sum_i \boldsymbol{p}_i^2}. \tag{22}$$

The temperature will therefore be a constant of motion if ζ is computed from the above equation at every time step.

Because the above constraints are applied in differential form, the constrained quantities are constants of motion. To be constant at the correct values, appropriate initial values must be programmed into the model. The molecules were therefore initially constructed with appropriate bond lengths and the temperature was rescaled as required. Even so, numerical errors from the inexact solution of the equations of motion and roundoff errors introduced by the computer cause the constrained distances to eventually deviate from the desired values. In order to correct for this drift, the penalty function approach and nonlinear minimization method of Edberg *et al.* [9] was implemented. Whenever the values of the bond length or velocity penalty functions became larger than an appropriate tolerance limit, the minimization procedure was invoked to reassemble the sites within the molecules at appropriate loci.

Time-Saving Algorithms

The following modifications were implemented into the NEMD algorithm to reduce the required CPU time:

1. The Runge-Kutta integration method used in the original code was replaced by a fourth-order predictor-corrector (PC) method to avoid multiple force calculations per time step. It was also found that the predictor-corrector method made the integration more stable, permitting a 50% increase in the small step size generally used with the original code. There is a trade-off between larger step size and the increasing frequency at which bond lengths must be re-optimized through the penalty functions. The stability of the PC algorithm permitted the increased step size without increasing the frequency at which the penalty functions were exceeded.

2. A neighbor list (NL) with automatic update was also implemented. Because of the boundary conditions used in the SLLOD algorithm, neighbor lists have proven difficult to implement. In this work, the SLLOD periodic boundaries were applied to the centers of mass of the molecules. When a molecule crosses a cell boundary in the y direction, the x coordinate of the image particle inserted through the opposite y boundary is shifted an amount which depends upon the relative time and shear that has occurred. If a regular neighbor update time is used, a particle may be shifted into

a new neighborhood list between updates by this SLLOD boundary condition. It is therefore essential that the update be performed automatically as necessary, rather than at preset intervals. In this work, a spherical neighborhood buffer radius was taken as $r_c + 0.3\sigma$ where r_c is the potential cutoff distance (2.5σ here). For each molecule, center-of-mass displacements were vectorally added at each time step and the maximum displacement of any one molecule since the last neighbor update was determined. The displacement vectors also included effects due to shear and the shift imposed by y-boundary crossings. This is essential since the SLLOD periodic boundary condition may shift the x coordinate of a molecule any fraction of the cell length when it crosses the y boundary. When twice the maximum displacement exceeded the neighbor buffer distance, a neighbor update was initiated. The effectiveness of the neighbor list depends considerably upon the shear rate and temperature of the simulation. Larger temperatures and higher shear rates require a higher update frequency. At the lower shear rates, the neighbor list required updating only about every 30 time steps while average updates were required two to three times more frequently at the higher shear rates.

3. A multiple time step (MTS) method [28] was also introduced to minimize time spent evaluating pair forces in the main force loop. The force on a molecule can be divided into primary $\boldsymbol{F}^p$ and secondary $\boldsymbol{F}^s$ forces. Neighbors of a molecule are considered primary if they are within a distance r_p. In this work r_p was taken as 1.2σ. The dynamics of a molecule are dominated by its primary neighbors. It feels a rapidly changing primary force resulting from collisions with its nearest-neighbor or "cage" molecules and a weaker secondary force (from molecules for which $r_p < r < r_c$) which changes much more slowly in time. Implementation of the MTS method is straightforward but does require considerable additional programming. At time t, neighbors of each particle are classified as primary or secondary and all forces are calculated in the normal way. Additionally, the time derivatives of the secondary forces are calculated. This involves little additional computation time since the derivatives of position required in these calculations are already available from the predictor algorithm. At each of the next m-1 time steps, the total secondary force on molecule i is estimated from a Taylor series

$$\boldsymbol{F}_i^s\,[t + m(\delta t)] \simeq \boldsymbol{F}_i^s(t) + m(\delta t)\dot{\boldsymbol{F}}_i^s(t) + \frac{1}{2}m^2(\delta t)^2\ddot{\boldsymbol{F}}_i^s(t). \tag{23}$$

The method in effect uses two separate time steps – the usual δt for updating primary forces and $m(\delta t)$ for explicitly updating secondary forces. Time derivatives of the secondary forces and virial, required for implementation and property calculations, are available in reference [10].

Table 4 Relative CPU times for various time-saving algorithms

algorithm	*CPU time relative to original code*
original code	1.00
PC	0.53
PC + NL	0.35
PC + NL + MTS	0.14
PC + NL + MTS + expanded step size	0.09

Each of the above modifications was individually tested by comparison of simulations with and without the new algorithm for over 50 000 time steps. In this work, secondary forces were explicitly reevaluated every seven steps ($m = 7$). A summary of the relative CPU savings for each of the above modifications is contained in Table 4.

Acknowledgement

The code used in this work was modified from the code used by Edberg *et al.* [8, 9]. We are grateful to Roger Edberg and Dennis Evans for use of their code. Gratitude is also expressed to NIST for the sabbatical opportunity of RLR and his use of the supercomputer during that time. The very helpful suggestions and comments of Howard Hanley and Dan Friend, both of NIST, are also appreciated.

References

[1] M.P. Allen and D.J. Tildesley, *Computer simulation of liquids,* Clarendon, Oxford, 987.
[2] J.J. Erpenbeck, "Shear viscosity of the hard-sphere fluid via nonequilibrium molecular dynamics", *Phys. Rev. Lett.* **52**, 1333 (1984).
[3] D.J. Evans and H.J.M. Hanley, "Viscosity of a mixture of soft spheres", *Phys. Rev. A* **20**, 1648 (1979).
[4] L.V. Woodcock and M.F. Edwards, *Inst. Chem. Eng. Symp. Ser. No. 91,* Birmingham, March 1983, p. 107.
[5] D.J. Evans and R.O. Watts, "Shear-dependent viscosity in simple fluids", *Chem. Phys.* **48**, 321 (1980).
[6] D.M. Heyes, "Shear thinning and thickening of the Lennard-Jones liquid", *J. Chem. Soc., Faraday Trans. II* **82**, 1365 (1986).
[7] B.Y. Yang and P.T. Cummings, "Nonequilibrium molecular dynamics calculation of the shear viscosity of carbon dioxide", *Int. J. Thermophys.* **10**, 929 (1989).
[8] R. Edberg, G.P. Morriss and D.J. Evans, "Rheology of *n*-alkanes by nonequilibrium molecular dynamics", *J. Chem. Phys.* **86**, 4555 (1987).
[9] R. Edberg, D.J. Evans and G.P. Morriss, "Constrained molecular dynamics: simulations of liquid alkanes with a new algorithm", *J. Chem. Phys.* **84**, 6933 (1986).
[10] R.L. Rowley and J.F. Ely, "Nonequilibrium molecular dynamics simulations of structured molecules. I. Isomeric effects of the viscosity of butanes", *Mol. Phys.* (in press).
[11] J.-P. Ryckaert and A. Bellemans, "Molecular dynamics of liquid alkanes", *Discuss. Faraday Soc.* **66**, 95 (1978).
[12] G. Maréchal, J.-P. Ryckaert and A. Bellemans, "The shear viscosity of *n*-butane by equilibrium and non-equilibrium molecular dynamics", *Mol. Phys.* **61**, 33 (1987).
[13] D.W. Rebertus and B.J. Berne, "A molecular dynamics and Monte Carlo study of solvent effects on the conformational equilibrium of *n*-butane in CCl_4", *J. Chem. Phys.* **70**, 3395 (1979).
[14] J.-P. Ryckaert and A. Bellemans, "Molecular dynamics of liquid *n*-butane near its boiling point", *Chem. Phys. Lett.* **30**, 123 (1975).
[15] D. Brown and J.H.R. Clarke, "The rheological properties of model liquid *n*-hexane determined by nonequilibrium molecular dynamics", *Chem. Phys. Lett.* **98**, 579 (1983).
[16] G. Maréchal and J.-P. Ryckaert, "Atomic versus molecular description of transport properties in polyatomic fluids: *n*-butane as an illustration", *Chem. Phys. Lett.* **101**, 548 (1983).
[17] D.J. Evans and G.P. Morriss, "Nonlinear-response theory for steady planar Couette flow", *Phys. Rev. A* **30**, 1528 (1984)
[18] D.J. Evans and G.P. Morriss, "Non-Newtonian molecular dynamics", *Comput. Phys. Repts.* **1**, 297 (1984).
[19] J.-P. Ryckaert, G. Ciccotti and H.J.C. Berendsen, "Numerical integration of the Cartesian equations of motion of a system with constraints: molecular dynamics of *n*-alkanes", *J. Comput. Phys.* **23**, 327 (1977).
[20] D.J. Evans, W.G. Hoover, B.H. Failor, B. Moran and A.J.C. Ladd, "Nonequilibrium molecular dynamics via Gauss's principle of least constraint", *Phys. Rev. A* **28**, 1016 (1983).
[21] K. Kawasaki and J.D. Gunton, "Theory of nonlinear transport processes: nonlinear shear viscosity and normal stress effects", *Phys. Rev. A* **8**, 2048 (1973).
[22] D.J. Evans, "Computer 'experiment' for nonlinear thermodynamics of Couette flow", *J. Chem. Phys.* **78**, 3297 (1983).

[23] D.J. Evans, H.J.M. Hanley and S. Hess, "Non-Newtonian phenomena in simple fluids", *Phys. Today* **37**, 26 (1984).
[24] D.E. Diller and L.J. Van Poolen, "Measurements of the viscosities of saturated and compressed liquid normal butane and isobutane", *Int. J. Thermophys.* **6**, 43 (1985).
[25] P.A. Wielopolski and E.R. Smith, "Dihedral angle distribution in liquid *n*-butane: molecular dynamics simulations", *J. Chem. Phys.* **84**, 6940 (1986).
[26] T.A. Weber, "Simulation of *n*-butane using a skeletal alkane model", *J. Chem. Phys.* **69**, 2347 (1978).
[27] A. Bañón, F.S. Adán and J. Santamaría, "The effect of intermolecular potential model on the structure and conformational equilibrium of liquid *n*-butane", *J. Chem. Phys.* **83**, 297 (1985).
[28] W.B. Street, D.J. Tildesley and G. Saville, "Multiple time-step methods in molecular dynamics", *Mol. Phys.* **35**, 639 (1978).